

Tightly Coupled GNSS/INS Integration Via Factor Graph and Aided by Fish-eye Camera

Weisong Wen, Xiwei Bai, Yin Chiu Kan, and Li-Ta Hsu*

Abstract— GNSS/INS integrated solution has been extensively studied over the past decades. However, its performance relies heavily on environmental conditions and sensor cost. The GNSS positioning can obtain satisfactory performance in the open area. Unfortunately, its accuracy can be severely degraded in a highly urbanized area, due to the notorious multipath effects and none-line-of-sight (NLOS) receptions. As a result, excessive GNSS outliers occur, which causes huge error in GNSS/INS integration. This paper proposes to apply a fish-eye camera to capture the sky view image to further classify the NLOS and line-of-sight (LOS) measurements. In addition, the raw INS and GNSS measurements are tightly integrated using a state-of-the-art probabilistic factor graph model. Instead of excluding the NLOS receptions, this paper makes use of both the NLOS and LOS measurements by treating them with different weightings. Experiments conducted in typical urban canyons of Hong Kong showed that the proposed method could effectively mitigate the effects of GNSS outliers, and an improved accuracy of GNSS/INS integration was obtained, when compared with the conventional GNSS/INS integration.

Index Terms— GNSS; INS; Camera; Integration; Factor Graph; Positioning; Autonomous Driving

I. INTRODUCTION

Over the past decade, there is an increasing demand for accurate and absolute positioning service in many applications, such as autonomous driving vehicles (ADV) [1] and unmanned aerial vehicle (UAV) [2]. Global navigation satellite system (GNSS) [3] currently remains the principal mean of providing globally referenced positioning in the integrated navigation system. With the availability of multiple satellite constellations, GNSS can provide satisfactory performance in the open area. However, the positioning error can go up to 50 meters in the highly urbanized city such as Hong Kong [4]. The inertial navigation system (INS) can provide high-frequency relative acceleration and angular velocity measurements. However, the INS is subject to the long-term drift. Therefore, the GNSS is usually integrated [5-8] with inertial navigation system (INS) to improve the performance of GNSS stand-alone method, due to their complementary properties [3]. Unfortunately, the GNSS/INS integration still cannot provide satisfactory accuracy in urban canyons where there are excessive GNSS positioning outliers. The main reason behind is that the GNSS signal blockage and reflection caused by the surrounding buildings [9] and dynamic objects [10] lead to the multipath

effects and none-line-of-sight (NLOS) receptions [11]. In summary, excessive unexpected GNSS outliers (see Figure 1) are the dominant difficulty for the accuracy of GNSS/INS integration. The major research streams to improve the performance of the GNSS/INS integration include: 1) develop better sensor integration framework to resist the effects of GNSS outliers (due to NLOS receptions and multipath effects). 2) mitigate the standalone GNSS positioning using innovative signal processing methods.

The recent GNSS/INS integration frameworks were extensively reviewed in [12] and detailed in [3]. The three most common integration solutions are the loosely-coupled [13], the tightly-coupled [14] and the ultra-tightly [15] coupled integrations. The ultra-tightly coupled integration makes use of the baseband signal processing of GNSS receiver such as the tracking loops, which is usually not accessible for commercial GNSS receivers. The major difference between the tightly coupled and loosely coupled solution is the domain of GNSS measurements used in the GNSS/INS integration scheme. In the loosely coupled GNSS/INS integration, the position and velocity from GNSS receiver are directly incorporated with the INS navigation solution. Whereas, the tightly coupled scheme uses the GNSS raw measurements, such as pseudorange. The tightly-coupled GNSS/INS integration can obtain better performance as shown in [14]. The main reason is that the quality of GNSS measurements can be modeled in a more accurate way [14]. The Kalman filter [16] and its variants [7, 17] are commonly used to integrate the GNSS/INS. These filter-based sensor integrations estimate the optimal posterior of the state based on the measurements at current epoch and the state at last epoch. In other words, the filter-based method is not able to fully make use of the advantage of historical states and observations. Recently, the factor graph [18] which is popular in the robotics field is employed to integrate GNSS/INS in a loosely-coupled manner [19] and tightly coupled manner [20]. Unfortunately, only simulated data are evaluated both in [19] and [20]. The result shows that the tightly-coupled GNSS/INS integration using factor graph optimization obtains better performance than the filter-based method [20]. The main reason is that the factor graph based GNSS/INS integration makes use of the historical information to estimate the optimal state sets which can increase the resistance against the unexpected GNSS outliers. However, this increased resistance relies on the uncertainty estimation of GNSS measurements. In fact, majority of the GNSS measurements are NLOS receptions in urbanized areas, such as Hong Kong and New York. The

Weisong Wen, Xiwei Bai, Yin Chiu Kan and L.T. Hsu, is with Hong Kong Polytechnic University, Hong Kong (e-mail: lt.hsu@polyu.edu.hk).

uncertainty of NLOS reception cannot be effectively modeled simply based on the conventional elevation angle and signal to noise ratios (SNR) based model [21] as NLOS tends to increase the uncertainty.

Instead of improving GNSS/INS integration from the integration scheme aspect, researchers propose different innovative signal processing methods, such as the sensitivity tracking loops [22], cooperative GNSS positioning [23, 24], the popular 3D map aided GNSS (3DMA GNSS) [25-29], 3D LiDAR aided GNSS [10, 11] and camera aided GNSS [30, 31]. The 3DMA GNSS could effectively improve the performance of GNSS positioning by excluding the NLOS receptions or correcting the NLOS receptions. A well-known method, GNSS shadow matching, was studied to match the measured satellite visibility with the predicted satellite visibility of hypothesized positions [32-34]. However, the performance of shadow matching relies on the quality of satellite visibility classification and initial guess of GNSS receiver. A likelihood-based 3DMA GNSS method, which modeled the measurement uncertainty to mitigate the NLOS effects, was also proposed to provide accurate positioning in the along-street direction [35]. Due to the complementarity of the shadow matching and the likelihood-based 3DMA GNSS, their integration was recently studied [36] to obtain better performance. Another stream of range-based 3DMA GNSS method was to correct the NLOS affected measurement for GNSS positioning [28, 37-39]. These methods were proposed to simulate the signals transmission routes using the ray-tracing method. However, they rely on the initial guess of the GNSS receiver's position and the availability of 3D maps, which are the main difficulties for implementation. The recently proposed 3D LiDAR aided GNSS could effectively improve the GNSS positioning by excluding [10] or correcting [11] the NLOS receptions. However, only part of the NLOS could be detected due to the limited field of view (FOV) of 3D LiDAR sensor. To detect the visibility of satellites, the researchers employed omnidirectional and fisheye cameras [30, 40-42] to detect the sky views of the environment. NLOS receptions could be detected with the detected sky views and decent improvements were obtained. Similar researches [43, 44] were conducted recently and the improved GNSS positioning was integrated with visual simultaneous localization and mapping [45]. However, these methods tended to exclude the NLOS receptions from further GNSS positioning which was not applicable in the dense urban areas. As the excessive NLOS exclusion could severely distort the geometry distribution of satellites. According to our research in [46], NLOS exclusion could conversely increase the GNSS positioning error in dense urban. Therefore, NLOS exclusion is not preferable for applications in urban canyons.

In summary, the factor graph-based tightly-coupled GNSS/INS integration obtained the best performance among all the sensor integration frameworks. However, it could not provide satisfactory accuracy when there were excessive unexpected GNSS NLOS measurements. In other words, insufficient modeling of NLOS receptions was the major difficulty. To solve this problem, this paper proposes to tightly

integrate GNSS/INS using the factor graph with the aid of fish-eye camera detecting NLOS reception. In this case, the potential GNSS outliers can be modeled subsequently. Instead of excluding the NLOS receptions, this paper makes use of both the NLOS and LOS measurements by treating them with different weightings. Finally, we validate the proposed method in typical urban areas of Hong Kong.

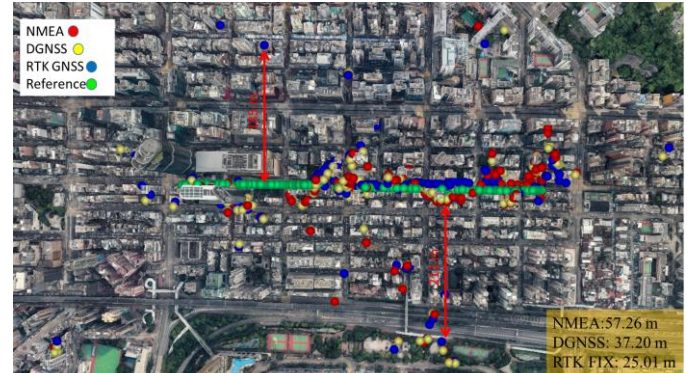


Fig. 1. GNSS positioning outliers: illustration of the performance of different GNSS positioning methods in different urban scenarios of Hong Kong. NMEA denotes the solution provided by GNSS commercial receiver. Differential GNSS (DGNSS) and real-time kinematics (RTK) are the state-of-the-art solution provided by GNSS open-source code, RTKLIB [47].

The rest of the paper is organized as following: In Section II, we discuss the overview of the proposed method. The LOS/NLOS classification and uncertainty modeling based on the fish-eye camera is presented in Section III. The proposed GNSS/INS integration is presented in Section IV before the experiment result is given in Section V. Finally, the conclusion of this study is summarized in Section VI.

II. OVERVIEW OF THE PROPOSED METHOD

The flowchart of the proposed method is shown in Figure 2. Firstly, a fish-eye camera is employed to capture the sky view image. The image segmentation is applied to separate the sky-view into sky and non-sky areas. With the aid of the globally referenced heading angle provided by an attitude and heading reference system (AHRS), which is a system integrated by INS and magnetometer. The coordinate of sky-view image can be transformed into the local coordinate (or we call it local frame). The AHRS used in this paper is a 9-axis product which consists of accelerometer, gyroscope, and magnetometer. It can output the absolute orientation. Secondly, the LOS/NLOS satellites can be classified based on the transformed binary images. Thirdly, the potential uncertainty of LOS/NLOS measurements is estimated using a scaled weighting scheme. Finally, the raw INS measurements, both the raw LOS and NLOS satellite measurements, are tightly integrated using a probabilistic factor graph model. The major contributions of this paper are listed as follows:

- (1) This paper employs the fish-eye camera to classify the LOS/NLOS measurement to further re-weight LOS and NLOS satellites.
- (2) This paper employs the state-of-the-art factor graph to integrate the GNSS/INS.

(3) This paper evaluates performance of multiple GNSS standalone and tightly-coupled GNSS/INS integrations in typical urban canyons of Hong Kong.

We believe that the proposed method in this paper can have a positive impact on both the academic and the industrial field of ADV.

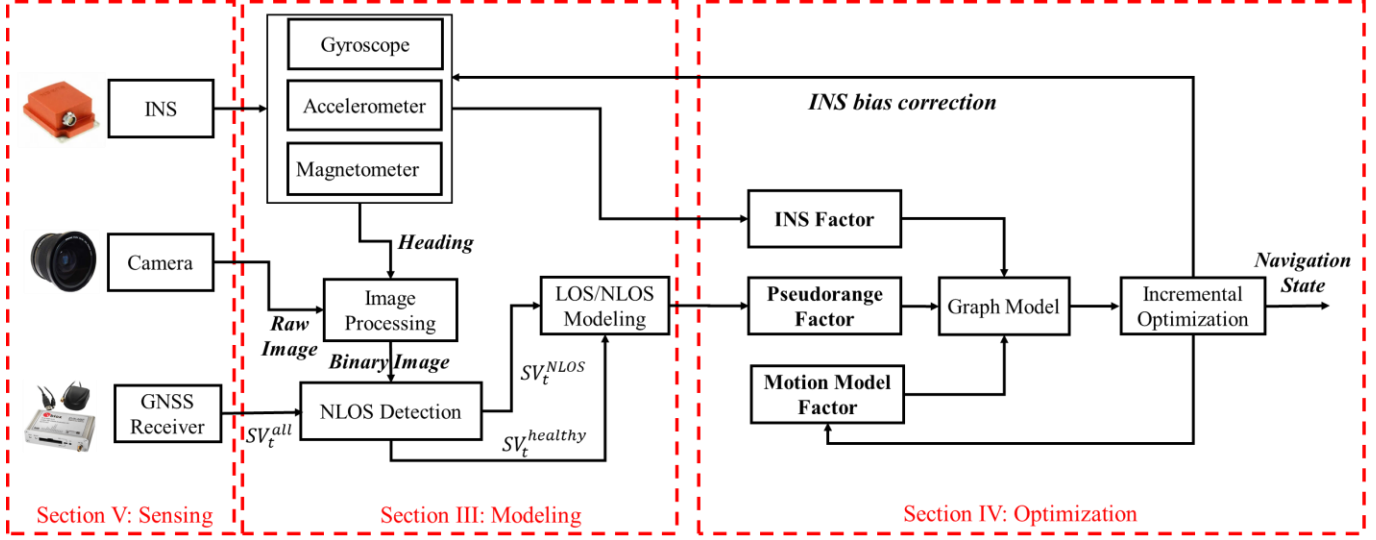


Fig. 2. Flowchart of the proposed GNSS/INS aided by fish-eye camera integration method which includes three parts: sensing, modeling, and optimization.

III. LOS/NLOS CLASSIFICATION AND MODELING

This section presents the classification of the satellite visibility in subsection A. The modeling of GNSS LOS and NLOS measurements are introduced in subsection B subsequently.

A. LOS/NLOS Classification Using Fish-eye Camera

The sky-view image captured from the fish-eye camera can effectively represent the geometry distribution of surrounding objects, such as buildings, tall dynamic vehicles, and trees, etc. To identify the LOS/NLOS using the sky-view image, four steps are proposed which can be seen in Figure 3: 1) transform the raw sky-image from body frame [3] to local frame [3] with the aid of heading angle from the AHRS. 2) segment the sky-view image and separate the sky and non-sky areas. 3) project the satellite onto the segmented image based on the satellite elevation and azimuth angles. 4) identify the satellite visibility based on the segmented image and satellite position in the image.

Step 1: The raw image from the fish-eye camera is taken in the body frame. In 3DMA GNSS [27], the 3D building models are usually projected onto the skyplot [48] together with the satellite to further identify whether the satellite is blocked by buildings. In this paper, we propose to directly project the satellite onto the image to identify the satellite visibility. Therefore, the image in the body frame should be transformed to the same frame as a satellite in the local frame. Assuming that the fish-eye camera is sky-pointing, only the globally referenced heading (τ_h) of the vehicle (provided by INS) is required to transform the image into the local frame.

Step 2: To separate the sky and non-sky area, we first transform the colored image to grayscale image. Then, the grayscale image is transformed to a binary image with an

adaptive threshold. The noisy points inside the binary image are filtered using a median filtering algorithm. These functions are conducted using OpenCV [49] library. The binary image is shown in Figure 3 (b). If the satellite locates inside the sky area, the satellite is visible to the GNSS receiver and vice versa.

Step 3: To identify the satellite visibility based on the processed image in Step 2, the satellite needs to be projected on the same coordinate system. The illustration of projecting satellite onto the image is shown in Figure 3 (c) which is a typical fish-eye projection model [50]. For each satellite associated with specific azimuth and elevation angles, it possesses a pixel position inside the sky view image. We assume that the optical center of the camera is zenith pointing. To determine the position of the satellite inside the image, we need, 1) The distance, r_{pix} , from the center of the sky-view image in pixels which is correlated to the elevation angle, ϕ_{sat} , of the satellite, and 2) The azimuth angle of the satellite.

Assume that the satellite is projected onto the image plane shown in Figure 3 (c), the image coordinate system is inside the image plane. The r_{pix} shown in Figure 3 (c) indicates the distance between the satellite position in the image and center of the image. The r_{pix} is determined by the satellite elevation angle and the focal length (f_c) of the fisheye camera. The angle θ satisfies:

$$\theta = \frac{\pi}{2} - \phi_{sat} \quad (1)$$

Thus, we have r_{pix} being formulated as follows [50]:

$$r_{pix} = 2 \cdot f_c (\theta/2) \quad (2)$$

Given the center of the sky-view image in a pixel position (x_c, y_c) , the position of the given satellite inside the sky view image can be formulated as (x_s, y_s) :

$$x_s = x_c + r_{pix} \cos(\tau_h + \alpha_{sat}) \quad (3)$$

$$y_s = y_c - r_{pix} \sin(\tau_h + \alpha_{sat}) \quad (4)$$

where the α_{sat} is the azimuth angle of the satellite.

Step 4: After the satellite is projected onto the sky-view image as shown in Figure 3 (d), we propose a searching method to identify the satellite visibility. For a given satellite (see Figure 3 (d)) located inside a sky-view image, we propose to identify the visibility using Algorithm 1. $V_{threshold}$ indicates the threshold of the mean pixel value and is experimentally determined. A satellite visibility classification result is shown in Figure 4. The satellites are projected onto the image with the red and green circles denoting the NLOS and healthy measurements, respectively.

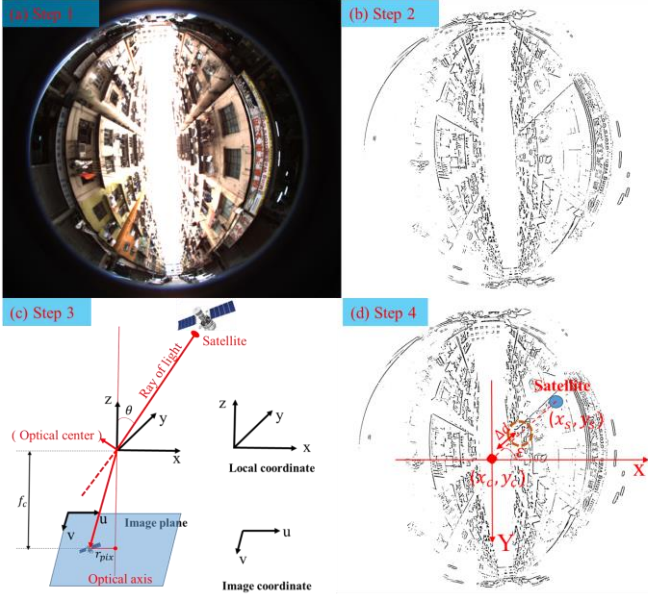


Fig. 3. Illustration of the proposed method to classify satellite visibility by fisheye camera. Four steps are 1) Coordination transformation from body to local frames, 2) Segmentation of sky and non-sky area, 3) Projection of satellites in image coordinate and 4) Identification of satellite visibility.

Algorithm 1: Satellite Visibility Identification

Input: binary image I_t as shown in Figure 3 (d), satellite position (x_s, y_s) in pixels inside the image, radius of the searching circle: R_s .

Output: satellite visibility st_v (visible: $st_v = 1$, invisible: $st_v = 0$)

S1: initialize the searching point (x_d, y_d) starting from the center $((x_c, y_c))$ of the image I_t , $st_v = 1$, the searching direction denoted by angle ε (see Figure 3 (d)).

S2: given a constant incremental value Δd , the searching

point is updated as follows:

$$x_d = x_d + \Delta d \cos(\varepsilon) \quad (5)$$

$$y_d = y_d - \Delta d \sin(\varepsilon) \quad (6)$$

S3: given the searching point (x_d, y_d) as the center of the searching circle, calculate the mean of pixel values of all the points inside the searching circle as follows:

$$\bar{V} = \sum_{i=1}^m I_t(x_{d,i}, y_{d,i}) \quad (7)$$

$I_t(x_{d,i}, y_{d,i})$ represents the pixel value of the point i inside the searching circle with radius of R_s .

S4: if $\bar{V} > V_{threshold}$, set st_v to 0.

S5: Repeat Steps 2 and 3 until the searching point reaches the position (x_s, y_s) of the given satellite.

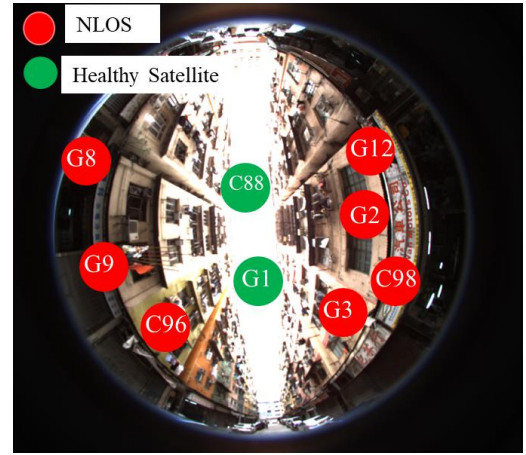


Fig. 4. Illustration of satellite visibility classification result.

B. LOS/NLOS Uncertainty Modeling

In terms of the measurements from the GNSS receiver, each pseudorange measurement ρ_n is written as follows [51].

$$\rho_n = R_n + c(\delta t^r - \delta t_n^{sv}) + I_n + T_n + \varepsilon_n \quad (8)$$

where R_n is the geometric range between the satellite and the GNSS receiver. δt_n^{sv} denotes the satellite clock bias. δt^r indicates the receiver clock bias. I_n represents the ionospheric delay distance; T_n indicates the tropospheric delay distance. ε_n represents the errors caused by the multipath effects, NLOS receptions, receiver noise, antenna delay, and so on. The ionospheric delay and tropospheric delay can be modeled using specific models [52]. Therefore, the majority of the uncertainty in pseudorange measurements is caused by the multipath effects and NLOS receptions in ε_n . The satellite with a lower elevation angle and smaller signal to noise ratio (SNR) has higher possibility to be contaminated by the NLOS errors [4]. Therefore, the pseudorange uncertainty modeling based on satellite elevation angle and SNR is studied in [21, 53]. The weighting scheme in [53] shows satisfactory performance in open area. However, the scheme may not work in dense urban as the NLOS can possess high elevation angle and SNR which

can be seen in our previous work in [42]. Moreover, this weighing scheme treat the LOS and NLOS in a same manner which is not preferable when the NLOS is identified. The weighting scheme in [21] employs a scaling factor to treat the LOS and NLOS with different weighting. Inspired by this, this paper proposes to model the uncertainty of LOS and NLOS using the weighting scheme in [53] and a scaling factor is added onto the scheme to treat the LOS and NLOS in a different manner. Assume that \mathbf{SV}_i represents the information from satellite i and $\mathbf{SV}_i = \{az_i, el_i, SNR_i, \rho_i\}$. az_i denotes the satellite azimuth angle. el_i represents satellite elevation angle, SNR_i indicates satellite SNR and ρ_i denote the pseudorange measurement. The weighting scheme in [53] is as follows:

$$\mathbf{W}_{LOS}^{(i)}(el_i, SNR_i) = \frac{1}{\sin^2 el_i} \left(10^{-\frac{(SNR_i - T)}{a}} \left(\frac{A}{10^{-\frac{(F-T)}{a}}} - 1 \right) \frac{(SNR_i - T)}{F - T} + 1 \right) \quad (9)$$

The parameter T indicates the threshold of SNR and is equal to $SNR_{threshold}$. Parameter a , A and F are experimentally determined. The weighting matrix \mathbf{W} is a diagonal matrix constituted by the weighting $\mathbf{W}^{(k)}(el_i, SNR_i)$. The weighting scheme treats LOS and NLOS using the same formula. We propose to add a scaling factor K to adapt the weighting scheme to treat LOS and NLOS differently as follows:

$$\mathbf{W}_{NLOS}^{(i)}(el_i, SNR_i) = K \cdot \mathbf{W}_{LOS}^{(i)}(el_i, SNR_i) \quad (10)$$

when the received signal is LOS, K is equal to 1. Whereas, when it is NLOS, K changes and is experimentally determined. In this paper, the variance (σ_p) of a pseudorange measurement is computed as $\sigma_p = 1/\mathbf{W}^{(i)}(el_i, SNR_i)$. In this case, the satellite visibility is classified, and corresponding uncertainty is modeled.

IV. GNSS/INS INTEGRATION USING FACTOR GRAPH

In general, the goal of the multi-sensor integration is to find the optimal posterior state given the measurements from sensors. Therefore, the sensor integration problem can be formulated as a typical maximum a posteriori (MAP) problem [54]. In this paper, the measurements include two parts, the GNSS raw measurements and INS measurements. Assuming that the GNSS measurements and INS measurements are independent of each other. We can formulate the GNSS/INS integration problem as:

$$\hat{\mathbf{x}} = \arg \max \prod_{t,i} P(\mathbf{z}_{t,i} | \mathbf{x}_t) \prod_t P(\mathbf{x}_t | \mathbf{x}_{t-1}, \mathbf{u}_t) \quad (11)$$

where $\mathbf{z}_{t,i}$ represents the GNSS raw measurements at epoch t and \mathbf{x}_t represents the system state at epoch t . The \mathbf{u}_t denotes the control input (INS measurements). $\hat{\mathbf{x}}$ is the optimal system state set [54]. In the conventional Bayes filter-based sensor integration scheme [55], the first order Markov assumption [55]

is applied. The GNSS/INS integration problem is formulated as:

$$\hat{\mathbf{x}} = \arg \max P(\mathbf{z}_{t,i} | \mathbf{x}_t) P(\mathbf{x}_t | \mathbf{x}_{t-1}, \mathbf{u}_t) \quad (12)$$

The main difference is that the Bayes filter-based method finds the best estimation of the current state only by considering: 1) the last state. 2) control input and measurements at the current epoch. It does not utilize the full advantage of the historical information. Conversely, the factor graph-based sensor integration [19] is studied to transfer the MAP problem into the non-linear optimization problem. It treats all the sensor measurements as constraints (edges) [19] associated with specific states (nodes) [19]. According to [18], the MAP problem can be expressed as:

$$\hat{\mathbf{x}} = \arg \max \prod_i f_i(\mathbf{x}_i) \quad (13)$$

where $f_i(\mathbf{x}_i)$ is a factor associated with measurements. \mathbf{x} denotes the states sets from first epoch to current epoch. Assuming that all the sensor noise is subject to Gaussian distribution, the negative logarithm of $f_i(\mathbf{x}_i)$ is proportional to the error function [18] associated with measurements.

The graph structure of the proposed GNSS/INS integration is shown in Figure 5. The state space of the system is represented as:

$$\mathbf{x}_k = (\mathbf{X}_{k,r}^{ecef}, \mathbf{V}_{k,r}^{ecef}, \mathbf{R}_{k,r}^{local}, \mathbf{B}_{k,r}^{body}, \delta_{k,r}^{clock})^T \quad (14)$$

where \mathbf{x}_k denotes the system state. $\mathbf{X}_{k,r}^{ecef} = (x_{k,r}^{ecef}, y_{k,r}^{ecef}, z_{k,r}^{ecef})$ represents the position of the GNSS receiver in ECEF coordinate [3] at given epoch k . $\mathbf{V}_{k,r}^{ecef} = (vx_{k,r}^{ecef}, vy_{k,r}^{ecef}, vz_{k,r}^{ecef})$ denotes the velocities of the GNSS receiver in ECEF coordinate, respectively. $\mathbf{R}_{k,r}^{local} = (\theta_{k,r}^{local}, \phi_{k,r}^{local}, \psi_{k,r}^{local})$ denotes the orientation in local frame. $\mathbf{B}_{k,imu}^{body} = (a_{k,x}^{body}, a_{k,y}^{body}, a_{k,z}^{body}, w_{k,x}^{body}, w_{k,y}^{body}, w_{k,z}^{body})$ denotes the bias of accelerometer and gyroscope in body (INS) frame. $\delta_{k,r}^{clock}$ denotes the GNSS receiver clock bias. In Figure 5, the black shaded rectangle represents the INS factor. The red and green shaded rectangles denote the LOS and NLOS satellites, respectively. The blue shaded box represents the state transition factor. The light green shaded box represents the INS accelerometer and gyroscope bias term.

The graph in Figure 5 includes all the historical observation measurements and states, which is one of the main differences between the conventional Kalman filter-based sensor integration [56] and the factor graph-based sensor integration.

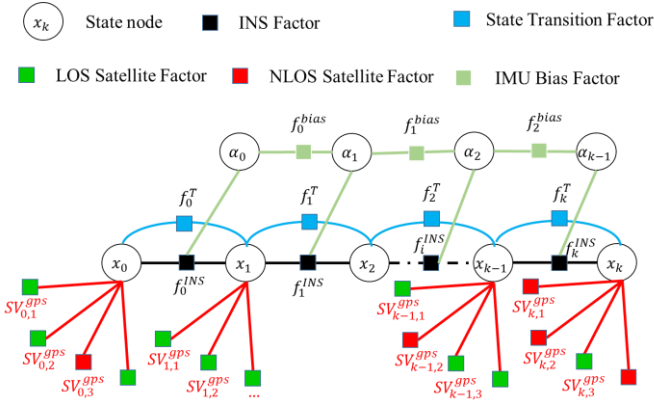


Fig. 5. Proposed GNSS/INS integration graph structure using a factor graph.

A. Motion Model Factor

We use a constant velocity model to constraint the two consecutive nodes (states). Based on the constant velocity model, the state transition (motion model) can be expressed as:

$$\mathbf{x}_{k+1} = h^{MM}(\mathbf{x}_k) + N(0, \Sigma_k^{MM}) \quad (15)$$

where \mathbf{x}_{k+1} denotes the state at given epoch $k+1$. $h^{MM}(\cdot)$ represents the motion model function. Σ_k^{MM} is the covariance matrix associated with the motion model whose noise is subject to Gaussian distribution. Based on the constant velocity motion model, the motion model function can be expressed as:

$$\mathbf{x}_{k+1} = h^{MM}(\mathbf{x}_k) = \begin{pmatrix} x_{k,r}^{ecef} + vx_{k,r}^{ecef} \cdot \Delta t \\ y_{k,r}^{ecef} + vy_{k,r}^{ecef} \cdot \Delta t \\ z_{k,r}^{ecef} + vz_{k,r}^{ecef} \cdot \Delta t \\ \delta_{k,r}^{clock} \\ \mathbf{B}_{k,r}^{bodyT} \end{pmatrix} \quad (16)$$

Δt is the time difference between the two states. Therefore, the error function (\mathbf{e}_k^{MM}) of the motion model factor can be expressed as:

$$\|\mathbf{e}_k^{MM}\|_{\Sigma_k^{MM}}^2 = \|\mathbf{x}_{k+1} - h^{MM}(\mathbf{x}_k)\|_{\Sigma_k^{MM}}^2 \quad (17)$$

B. INS Factor

As the INS applied in this paper is a 9-axis product, it can provide acceleration measurements, angular velocity measurements, and magnetometer measurements. Moreover, the orientation relative to the local frame can also be provided. The measurements from IMU is expressed as follows:

$$\mathbf{z}_k^{raw} = \begin{pmatrix} \theta_{k,AHRS}^{local}, \phi_{k,AHRS}^{local}, \psi_{k,AHRS}^{local}, wx_k^{body}, wy_k^{body}, wz_k^{bodyT} \\ , ax_k^{body}, ay_k^{body}, az_k^{body} \end{pmatrix} \quad (18)$$

where $wx_k^{body}, wy_k^{body}, wz_k^{body}$ represents the angular velocity in the INS frame. $ax_k^{body}, ay_k^{body}, az_k^{body}$ represents the

acceleration measurements in the INS frame. As the estimated state \mathbf{x}_k is in the global frame (ECEF), we need to transform the acceleration measurements from body frame to global frame based on the orientation and its position at last epoch. The transformed acceleration measurement $\mathbf{a}_k^{ecef} = (ax_k^{ecef}, ay_k^{ecef}, az_k^{ecef})^T$ is as follows [3]:

$$\mathbf{a}_k^{ecef} = \mathbf{R}_{GL} \mathbf{R}_{LB} (ax_k^{body} - a_{k,x}^{body}, ay_k^{body} - a_{k,x}^{body}, az_k^{body} - a_{k,x}^{body})^T \quad (19)$$

where \mathbf{a}_k^{ecef} is the acceleration measurements in ECEF frame. \mathbf{R}_{LB} is the transform matrix to transform the acceleration measurements from body frame to local frame based on the orientation. \mathbf{R}_{GL} is the transformation matrix to transform the acceleration measurement from local frame to global frame based on the \mathbf{x}_k with the \mathbf{R}_{GL} being expressed as follows:

$$\mathbf{R}_{GL} = \begin{pmatrix} -\sin(\varnothing_{lon}) & -\sin(\varnothing_{lat})\cos(\varnothing_{lon}) & \cos(\varnothing_{lat})\cos(\varnothing_{lon}) \\ \cos(\varnothing_{lon}) & -\sin(\varnothing_{lat})\sin(\varnothing_{lon}) & \cos(\varnothing_{lat})\sin(\varnothing_{lon}) \\ 0 & \cos(\varnothing_{lat}) & \sin(\varnothing_{lat}) \end{pmatrix} \quad (20)$$

where \varnothing_{lon} and \varnothing_{lat} represent the longitude and latitude which can be derived from \mathbf{x}_k in ECEF frame based on WGS84 geodetic system. Therefore, the error function for INS acceleration measurements can be expressed as follows:

$$\mathbf{e}_{k,acc}^{INS} = \begin{pmatrix} vx_{k+1,r}^{ecef} \\ vy_{k+1,r}^{ecef} \\ vz_{k+1,r}^{ecef} \end{pmatrix} - \begin{pmatrix} vx_{k,r}^{ecef} + ax_k^{ecef} \cdot \Delta t \\ vy_{k,r}^{ecef} + ay_k^{ecef} \cdot \Delta t \\ vz_{k,r}^{ecef} + az_k^{ecef} \cdot \Delta t \end{pmatrix} \quad (21)$$

where Δt is the time difference between two states and the covariance matrix for the INS factor is expressed as $\Sigma_{k,acc}^{INS}$. Similarly, we can obtain the error function for gyroscope as follows:

$$(\Delta\theta_{k,r}^{local}, \Delta\phi_{k,r}^{local}, \Delta\psi_{k,r}^{local}) = \mathbf{R}_{LB} ((wx_k^{body} - w_{k,x}^{body})\Delta t, (wy_k^{body} - w_{k,y}^{body})\Delta t, (wz_k^{body} - w_{k,z}^{body})\Delta t)^T \quad (22)$$

$$\mathbf{e}_{k,w}^{INS} = \begin{pmatrix} \theta_{k+1,r}^{local} \\ \phi_{k+1,r}^{local} \\ \psi_{k+1,r}^{local} \end{pmatrix} - \begin{pmatrix} \theta_{k,r}^{local} + \Delta\theta_{k,r}^{local} \\ \phi_{k,r}^{local} + \Delta\phi_{k,r}^{local} \\ \psi_{k,r}^{local} + \Delta\psi_{k,r}^{local} \end{pmatrix} \quad (23)$$

Moreover, the INS can also provide the orientation in the local frame as $\theta_{k,AHRS}^{local}, \phi_{k,AHRS}^{local}, \psi_{k,AHRS}^{local}$. Thus, the error function for AHRS measurements is as follows:

$$\mathbf{e}_{k,AHRS}^{INS} = \begin{pmatrix} \theta_{k+1,r}^{local} \\ \phi_{k+1,r}^{local} \\ \psi_{k+1,r}^{local} \end{pmatrix} - \begin{pmatrix} \theta_{k+1,AHRS}^{local} \\ \phi_{k+1,AHRS}^{local} \\ \psi_{k+1,AHRS}^{local} \end{pmatrix} \quad (24)$$

Therefore, the error function for INS is shown as follows:

$$\|e_k^{INS}\|_{\Sigma_k^{INS}}^2 = \|e_{k,acc}^{INS}\|_{\Sigma_k^{acc}}^2 + \|e_{k,w}^{INS}\|_{\Sigma_k^w}^2 + \|e_{k,AHRS}^{INS}\|_{\Sigma_k^{AHRS}}^2 \quad (25)$$

Σ_k^{acc} , Σ_k^w and Σ_k^{AHRS} are the covariance matrix associated with the acceleration, gyroscope and AHRS measurements, respectively.

C. GNSS Pseudorange Factor

The GNSS receiver receives multiple signals from satellites at a given epoch k which can be expressed as:

$$\mathbf{SV}_k = \{\mathbf{SV}_{k,1}, \mathbf{SV}_{k,2}, \mathbf{SV}_{k,3}, \dots, \mathbf{SV}_{k,j}\} \quad (26)$$

The position of GNSS receiver is $\mathbf{X}_{k,r}^{ecef} = (x_{k,r}^{ecef}, y_{k,r}^{ecef}, z_{k,r}^{ecef})$. The position of satellite $\mathbf{SV}_{k,n}$ is represented as $\mathbf{x}_{SV,n}^{xyz} = (x_{SV,n}^{ecef}, y_{SV,n}^{ecef}, z_{SV,n}^{ecef})^T$. Therefore, we can obtain the predicted GNSS pseudorange measurement for satellite $\mathbf{SV}_{k,n}$ as:

$$h^p(\mathbf{SV}_{k,j}, \mathbf{X}_{k,r}^{ecef}) = \|\mathbf{x}_{SV,j}^{xyz} - \mathbf{X}_{k,r}^{ecef}\| + \delta_{k,r}^{clock} \quad (27)$$

where $h^p(*)$ is the measurement function of pseudorange measurement. $\mathbf{x}_{SV,j}^{xyz}$ is the position of satellite j . $\mathbf{X}_{k,r}^{ecef}$ is the position of the GNSS receiver at given epoch k . $\delta_{k,r}^{clock}$ is the receiver clock bias. In this paper, the earth rotation and atmosphere delay are calculated in advance using the model detailed in [53]. The measured pseudorange from GNSS receiver is expressed as $\rho_{SV,n}$ and is given by the $h^p(\mathbf{SV}_{k,j}, \mathbf{X}_{k,r}^{ecef})$ and additional Gaussian noise. We can have the following formulation:

$$\rho_{SV,n} = h^p(\mathbf{SV}_{k,j}, \mathbf{X}_{k,r}^{ecef}) + N(0, \sigma_p^2) \quad (28)$$

where σ_p is the uncertainty of the given satellite measurement $\rho_{SV,n}$. The LOS/NLOS and their uncertainty is classified in Section III with $\sigma_{LOS,p}$ for LOS satellite and $\sigma_{NLOS,p}$ for NLOS satellite. Therefore, we can compute the error function for a given satellite measurement $\rho_{SV,j}$ as follows:

$$\|e_{k,j}^p\|_{\sigma_p^2}^2 = \|\rho_{SV,j} - h^p(\mathbf{SV}_{k,j}, \mathbf{X}_{k,r}^{ecef})\|_{\sigma_p^2}^2 \quad (29)$$

D. Efficient Incremental Optimization

Regarding the conventional GNSS single point positioning, the weighted least square method [3] is to make use of all the

satellite measurements at given epoch k to get the best posterior estimate of the GNSS receiver's position \mathbf{x}_k^{xyz} as follows:

$$\mathbf{X}_{k,r}^{ecef*} = \operatorname{argmin} \sum_j \|e_{k,j}^p\|_{\sigma_p^2}^2 \quad (30)$$

where $\mathbf{X}_{k,r}^{ecef*}$ is the optimal estimate of the GNSS receiver's position. If all the historical GNSS measurements are considered, the optimal GNSS receiver's position set $\mathbf{X}_k^{ecef} = \{\mathbf{X}_{1,r}^{ecef}, \mathbf{X}_{2,r}^{ecef}, \mathbf{X}_{3,r}^{ecef}, \dots, \mathbf{X}_{k,r}^{ecef}, \dots\}$ is estimated as follows:

$$\mathbf{X}_k^{ecef*} = \operatorname{argmin} \sum_{j,k} \|e_{k,j}^p\|_{\sigma_p^2}^2 \quad (31)$$

In this paper, we formulate three factors including the motion model factor, the INS factor and the GNSS pseudorange factor. Therefore, the optimal state set $\mathbf{X} = \{\mathbf{x}_1, \mathbf{x}_2, \mathbf{x}_3, \dots, \mathbf{x}_k, \dots\}$ can be solved as follows:

$$\mathbf{X}^* = \operatorname{argmin} \sum_{j,k} \|e_{k,j}^p\|_{\sigma_p^2}^2 + \|e_k^{MM}\|_{\Sigma_k^{MM}}^2 + \|e_{k,acc}^{INS}\|_{\Sigma_k^{acc}}^2 + \|e_{k,w}^{INS}\|_{\Sigma_k^w}^2 + \|e_{k,AHRS}^{INS}\|_{\Sigma_k^{AHRS}}^2 \quad (32)$$

To solve this optimization problem, this paper makes use of the ISAM2 [18] in GTSAM [57]. With the efficient incremental optimization feature [18] of ISAM2, the optimization problem can be conducted with real-time performance.

V. EXPERIMENT RESULTS

A. Experiment Setup

Two experiments were conducted in typical urban canyons of Hong Kong on 10 April 2019. The experimental scenes are shown in Figure 6. The figure on the left shows the test vehicle with all the sensors installed in a compact sensor kit. The figures in the middle and right show the tested urban canyons. The tested urban scenarios contain static buildings, trees and dynamic objects (double-decker bus, cars). According to our previous research [10], the double-decker bus could cause potential NLOS measurements.

In both experiments, a u-blox M8T GNSS receiver was used to collect raw GPS/BeiDou measurements at a frequency of 1 Hz. The sky-pointing fisheye camera was employed to capture the sky view image at a frequency of 10 Hz. The Xsens Ti-10 IMU was employed to collect data at a frequency of 100 Hz. In addition, the NovAtel SPAN-CPT, a GNSS RTK/INS (fiber optic gyroscopes) integrated navigation system, was used to provide the ground truth of positioning. All the data were collected and synchronized using the robot operation system (ROS) [58]. The coordinate systems between all the sensors were calibrated before the experiments. The parameters used in this paper are shown in Table I which are experimentally determined.



Fig. 6. Experimental vehicle and sensor setup in left-hand side figure. Tested scenarios of urban canyon 1 and 2.

We first analyzed the performance of GNSS standalone positioning performance using three single point positioning (SPP) methods as shown below. The objective of this analysis was to validate the effectiveness of the fish-eye camera in improving the GNSS standalone positioning.

(a) **LS**: least square (LS) method with all measurements given same weighting.

(b) **WLS**: weighted least square (WLS) method.

(c) **R-WLS**: WLS method with the aid of re-weighting scheme in equation (10).

Three GNSS/INS integrated positioning methods are also compared:

(1) **EKF**: EKF-based tightly coupled GNSS/INS [16].

(2) **FG**: Factor graph-based tightly-coupled GNSS/INS .

(3) **FGFC**: Factor graph-based tightly coupled GNSS/INS aided by fish-eye camera.

In the evaluation, the estimated state is in ECEF coordinate. We transform the positioning results from ECEF into the ENU coordinate. 2D positioning (north and east directions) performance of the three integrations are compared.

TABLE I
PARAMETER VALUES USED IN THIS PAPER

Parameters	$V_{threshold}$	Δd	K	f_c
Value	50	5 pixel	1.5	583
Parameters	a	A	F	
Value	30	32	10	

B. Evaluation in Urban Canyon 1 Experiment

1) GNSS Standalone Positioning

The GNSS standalone positioning result can be found in Table II. 15.51 meters of 2D mean positioning error is obtained by the conventional LS method. The maximum error reaches 48.6 meters. The mean positioning error decreases to 9.57 meters with the maximum error still being more than 40 meters using the WLS [53]. Moreover, the standard deviation decreases slightly. With the help of the fish-eye camera and the re-weighting scheme, the positioning error decreases to less than 9 meters. This improved result shows that applying

re-weighting scheme can lower the impacts of the NLOS measurements with the aid of fish-camera. The GNSS standalone positioning improvement is not dramatic (from 9.57 to 8.92 meters). However, the modeling of NLOS measurements is significant for further GNSS/INS integration which can be seen in next section.

The LOS/NLOS satellite numbers can be seen in Table III. The mean of LOS number (9.0) is larger than that of NLOS (4.6). More importantly, the standard deviation of NLOS satellite number is 2.57, which is larger than the satellite number of LOS being 1.92. The value for NLOS is larger regarding to the standard deviation of the LOS (1.92) and NLOS (2.57) satellites. Based on the classification by fish-eye camera, almost 33.83% of the satellites are NLOS measurements with the rest being the LOS. The minimum number of LOS satellites is only 4, which is not even enough for GNSS (GPS/Beidou) WLS calculation. Therefore, NLOS exclusion is not acceptable in this scenario. The maximum NLOS satellite number reaches 8.

The LOS/NLOS satellite distributions in 9 heuristically selected cases are shown in Figure 7. The positioning errors using the three SPP are shown in the figure. Several interesting findings are summarized in the followings. Firstly, the NLOS satellite numbers vary over epochs causing different magnitude of positioning error. For example, the errors are only 6.6 meters for LS and 4.9 meters for WLS with only 1 NLOS at Case A. Whereas, error of 47.6 meters for LS and 13.6 meters for WLS with 6 NLOS are obtained at Case E. Most importantly, the error is reduced to 4.1 and 9.1 meters using R-WLS at Cases A and E, respectively. Secondly, it is found that the re-weighting scheme could even deteriorate the result at Case F. The main reason is that it is caused by the truth that the LOS/NLOS classification based on fish-eye camera is not perfect. We can find that some satellites annotated with green arrows is misclassified at Case F, and at Case C. Our future work is to improve the image segmentation method to obtain better LOS/NLOS classification accuracy.

In short, the applied fish-eye can detect the NLOS measurements and improved GNSS standalone results are obtained by re-weighting the detected NLOS measurements.

TABLE II
POSITIONING PERFORMANCE OF THE GNSS SPSS IN URBAN CANYON 1

GNSS Positioning	LS	WLS	R-WLS
Mean error	15.51 m	9.57 m	8.92 m
Std	10.33	7.32	7.27
Maximum error	48.16 m	46.29 m	42.33 m

TABLE III
SATELLITE NUMBERS IN URBAN CANYON 1

Satellite	LOS	NLOS	LOS&NLOS
Mean number	9.0	4.6	13.63
Std	1.92	2.57	2.49
Max number	15	8	18
Min number	4	0	7
Percentage	66.17%	33.83%	100%

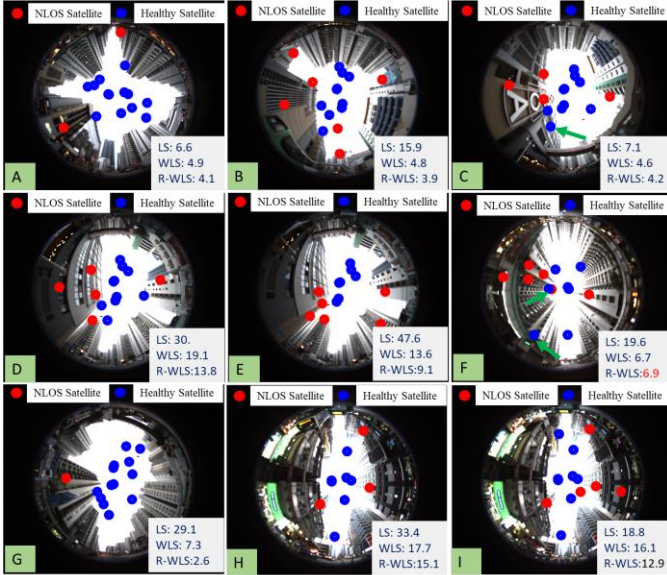


Fig. 7. The satellite visibilities at 9 heuristically selected cases.

2) GNSS/INS Integrated Positioning

After integrating the INS, the positioning results using the three listed GNSS/INS integrations are shown in TABLE IV. 8.31 meters of 2D mean positioning is obtained using the conventional EKF-based tightly coupled GNSS/INS integration. Moreover, the standard deviation is 7.24 meters. Its trajectory deviates the reference trajectory in some of the epochs as shown in Figure 8. The corresponding 2D positioning error can be seen in Figure 9. The maximum error is larger than 40 meters. After using the factor graph to integrate the GNSS/INS, the mean of positioning error decreases to about 4 meters. Moreover, the standard deviation also decreases from 7.24 to 3.19 meters, and the maximum error is 23.1 meters. From Figure 8, the majority of the large outliers are removed from the trajectories. The positioning errors are reduced almost

throughout the epochs which can be seen in Figure 9. With the help of the LOS/NLOS detection method aided by fish-eye camera, the mean 2D positioning error is reduced to 3.21 meters. Moreover, the standard deviation is also decreased to less than 2 meters. In addition, the maximum error is also reduced to 12.3 meters with less outliers.

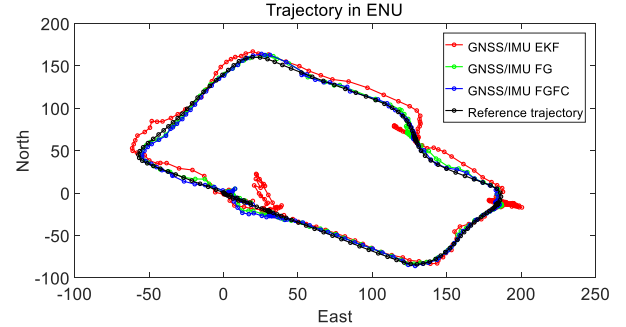


Fig. 8. Trajectories of the GNSS/INS integrations in urban canyon 1: the x- and y-axes denote the position in east and north directions, respectively.

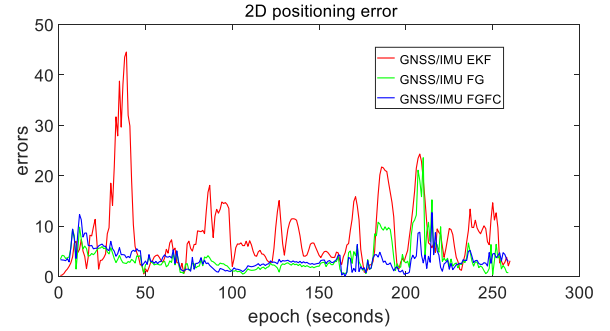


Fig. 9. 2D positioning error of the GNSS/INS integrations in urban canyon 1.

In short, the factor graph-based method can improve the positioning performance from 8.31 to 3.96 meters. However, the positioning error can still reach more than 20 meters in some epochs (e.g. epoch 200~210). The re-weighting of NLOS measurements can help to mitigate the larger outliers with all the positioning errors being less than 14 meters (see blue curve in Figure 9). The result shows that the re-modeling of NLOS is significant for mitigating GNSS/INS integration outliers. This is significant for autonomous driving localization, which requires high robustness.

TABLE IV
POSITIONING PERFORMANCE OF THE THREE METHODS IN URBAN CANYON 1

All data	EKF	FG	FGFC
Mean error	8.31 m	3.96 m	3.21 m
Std	7.24	3.19	1.96
Maximum error	44.2 m	23.1 m	12.3 m

C. Evaluation in Urban Canyon 2 Experiment

1) GNSS Standalone Positioning

To challenge the performance of the proposed method in denser urban (with larger percentage of NLOS measurements), we conduct the other experiment in urban canyon 2 with

narrower streets (see Figure 6), which is more challenging compared to urban canyon 1 situation. Although the denser urbanization, GNSS standalone positioning is obtained with the error being reduced from 8.57 m (WLS) to 8.12 m (R-WLS). The detailed results can be seen in Table V, which is similar to the improvement in urban canyon 1. The mean of LOS/NLOS satellite numbers and corresponding percentage are shown in Table IV. We can observe that the percentage (41.94%) of NLOS satellite are larger compared with the one (33.83%) in urban canyon 1. This means that there exists more reflected GNSS signals. The minimum NLOS number is 1 which means at least 1 NLOS measurement exists during the test. Interestingly, the minimum LOS number is only 2, which is not even enough for GNSS positioning. This again shows that re-using the NLOS is more preferable instead of NLOS exclusion.

TABLE V
POSITIONING PERFORMANCE OF THE GNSS SPSS IN URBAN CANYON 2

GNSS Positioning	LS	WLS	R-WLS
Mean error	11.7 m	8.57 m	8.12 m
Std	6.53	5.50	5.59
Maximum error	30.01 m	25.91 m	25.36 m

TABLE VI
SATELLITE NUMBERS IN URBAN CANYON 2

Satellite	LOS	NLOS	LOS&NLOS
Mean number	7.31	5.27	12.58
Std	2.63	1.77	3.21
Max number	13	8	18
Min number	2	1	6
Percentage	58.06%	41.94%	100%

2) GNSS/INS Integrated Positioning

The evaluated positioning result is shown in TABLE VII. 7.28 meters of 2D mean positioning is obtained using the EKF GNSS/INS integration. Moreover, the standard deviation is 4.41 meters. Interestingly, we can find that the mean positioning error of EKF-based tightly coupled GNSS/INS integration is smaller in urban canyon 2 (7.28 m) compared with the one in urban canyon 1 (8.31 m), although the percentage of NLOS is larger in urban canyon 2. According to our previous research in [4], the NLOS error caused is determined by three components: 1) the azimuth angle of satellite. 2) the elevation angle of satellite and 3) the distance between the GNSS receiver and potential reflector. Therefore, larger percentage of NLOS satellites do not necessarily cause larger GNSS positioning error as it also depends on the environment conditions (e.g. the distance between the GNSS receiver and signal reflector) shown in Figure 6. The urban canyon 1 has larger street width compared with urban canyon 2. Therefore, the test in urban canyon 1 can have even larger mean positioning error.

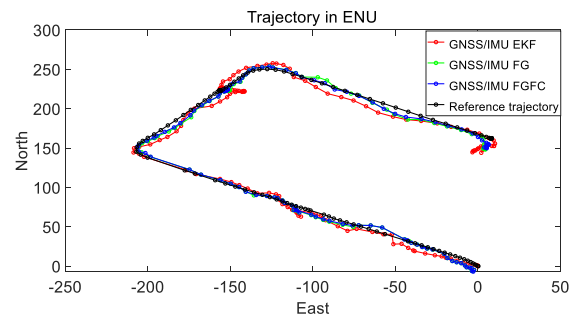


Fig. 10. Trajectories of the GNSS/INS integrations in urban canyon 2: the x- and y-axes denote the position in east and north directions, respectively.

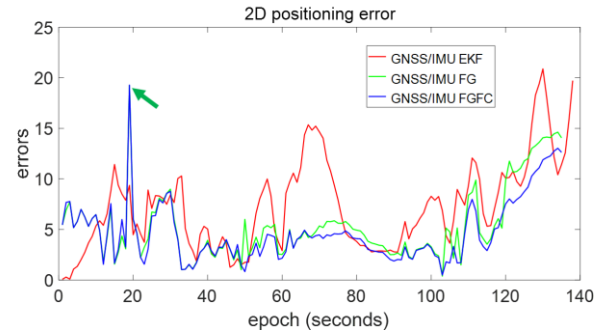


Fig. 11. 2D positioning error of the GNSS/INS integrations in urban canyon 2.

The trajectory and its corresponding 2D positioning error are shown in Figures 10 and 11, respectively. The maximum 2D error reaches 20.88 meters. Using the factor graph to integrate the GNSS/INS, the mean positioning error decreases to about 3.5 meters. Moreover, the standard deviation also decreases from 4.41 to 3.50 meters. The maximum error is 19.2 meters. Majority of the large outliers are removed from the trajectories. The positioning errors are reduced throughout most of the epochs, which can be seen in Figure 11. With the help of the LOS/NLOS detection and modeling aided by fish-eye camera, the mean 2D positioning error is reduced to 3.05 meters. Moreover, the standard deviation is also decreased to about 3 meters. Interestingly, we can find that the blue curve in Figure 11 peaks at the epoch 20 annotated by the green arrow. The main reason behind is due to the misclassification of LOS/NLOS measurements (see the illustration in Figure 7 Case F).

In short, the improved result again shows effectiveness of the proposed method. Compared to the EKF-based method, the proposed method can effectively remove the outliers.

TABLE VII
POSITIONING PERFORMANCE OF THE THREE METHODS IN URBAN CANYON 2

All data	EKF	FG	FGFC
Mean error	7.28 m	5.39 m	4.73 m
Std	4.41	3.50	3.06
Maximum error	20.88 m	19.2 m	19.1 m

VI. CONCLUSIONS

GNSS/INS integrated navigation is significant for systems with positioning requirements. However, the performance of GNSS/INS integration suffers from excessive unexpected GNSS outliers in dense urban areas. This paper proposes to tightly integrate GNSS/INS using the state-of-the-art factor graph. Moreover, we employ the fish-eye camera to detect NLOS receptions so that the GNSS outliers can be modeled. Instead of excluding the NLOS receptions, this paper makes use of both the NLOS and LOS measurements by treating them with different weightings. The experiments show that the proposed method can effectively improve the performance of GNSS/INS integration compared with the conventional GNSS/INS tightly coupled integration using EKF.

In urban canyon 1 experiment, the mean positioning error is reduced from 8.31 to 3.21 meters. In urban canyon 2 experiment, the mean positioning error is reduced from 7.28 to 4.73 meters. However, the remaining 2D positioning error is still not enough for autonomous driving vehicle. In the future work, we will integrate the LiDAR-based positioning into the proposed GNSS/INS fusion scheme. In addition, the sky and non-sky area separation method will be further improved in the future work.

REFERENCES

- [1] J. Levinson *et al.*, "Towards fully autonomous driving: Systems and algorithms," in *2011 IEEE Intelligent Vehicles Symposium (IV)*, 2011, pp. 163-168: IEEE.
- [2] R. Li, J. Liu, L. Zhang, and Y. Hang, "LiDAR/MEMS IMU integrated navigation (SLAM) method for a small UAV in indoor environments," in *2014 DGON Inertial Sensors and Systems (ISS)*, 2014, pp. 1-15: IEEE.
- [3] P. D. Groves, *Principles of GNSS, inertial, and multisensor integrated navigation systems*. Artech house, 2013.
- [4] L.-T. Hsu, "Analysis and modeling GPS NLOS effect in highly urbanized area," *GPS solutions*, vol. 22, no. 1, p. 7, 2018.
- [5] A. Angrisano, M. Petovello, and G. Pugliano, "GNSS/INS integration in vehicular urban navigation," *Proceedings of GNSS10 (Portland, OR, 21-24 Sep)*, The Institute of Navigation, 2010.
- [6] C. Fernández-Prades, P. Closas, and J. Vila-Valls, "Nonlinear filtering for ultra-tight GNSS/INS integration," in *2010 IEEE International Conference on Communications*, 2010, pp. 1-5: IEEE.
- [7] Y. Meng, S. Gao, Y. Zhong, G. Hu, and A. Subic, "Covariance matching based adaptive unscented Kalman filter for direct filtering in INS/GNSS integration," *Acta Astronautica*, vol. 120, pp. 171-181, 2016.
- [8] G. Zhang and L.-T. Hsu, "Intelligent GNSS/INS integrated navigation system for a commercial UAV flight control system," *Aerospace Science and Technology*, vol. 80, pp. 368-380, 2018.
- [9] Y. Wada, L.-T. Hsu, Y. Gu, and S. Kamijo, "Optimization of 3D building models by GPS measurements," *GPS solutions*, vol. 21, no. 1, pp. 65-78, 2017.
- [10] W. Wen, G. Zhang, and L.-T. Hsu, "Exclusion of GNSS NLOS receptions caused by dynamic objects in heavy traffic urban scenarios using real-time 3D point cloud: An approach without 3D maps," in *Position, Location and Navigation Symposium (PLANS), 2018 IEEE/ION*, 2018, pp. 158-165: IEEE.
- [11] G. Z. Weisong Wen, Li-ta Hsu, "Correcting GNSS NLOS by 3D LiDAR and Building Height," presented at the ION GNSS+, 2018, Miami, Florida, USA., 2018.
- [12] A. Angrisano, "GNSS/INS integration methods," *Dottorato di ricerca (PhD) in Scienze Geodetiche e Topografiche Thesis, Universita' degli Studi di Napoli PARTHENOPE, Naples*, vol. 21, 2010.
- [13] A. Solimeno, "Low-cost INS/GPS data fusion with extended Kalman filter for airborne applications," *Masters of Science, Universidade Technica de Lisboa*, 2007.
- [14] M. G. Petovello, *Real-time integration of a tactical-grade IMU and GPS for high-accuracy positioning and navigation*. Citeseer, 2003.
- [15] G. Gao and G. Lachapelle, "A novel architecture for ultra-tight HSGPS-INS integration," *Positioning*, vol. 1, no. 13, p. 0, 2008.
- [16] G. Falco, M. Pini, and G. Marucco, "Loose and tight GNSS/INS integrations: Comparison of performance assessed in real urban scenarios," *Sensors*, vol. 17, no. 2, p. 255, 2017.
- [17] Z. Tao, P. Bonnifait, V. Frémont, J. Ibanez - Guzman, and S. Bonnet, "Road - Centered Map - Aided Localization for Driverless Cars Using Single - Frequency GNSS Receivers," *Journal of Field Robotics*, vol. 34, no. 5, pp. 1010-1033, 2017.
- [18] M. Kaess, H. Johannsson, R. Roberts, V. Ila, J. J. Leonard, and F. Dellaert, "iSAM2: Incremental smoothing and mapping using the Bayes tree," *The International Journal of Robotics Research*, vol. 31, no. 2, pp. 216-235, 2012.
- [19] V. Indelman, S. Williams, M. Kaess, and F. Dellaert, "Factor graph based incremental smoothing in inertial navigation systems," in *2012 15th International Conference on Information Fusion*, 2012, pp. 2154-2161: IEEE.
- [20] W. Li, X. Cui, and M. Lu, "A robust graph optimization realization of tightly coupled GNSS/INS integrated navigation system for urban vehicles," *Tsinghua Science and Technology*, vol. 23, no. 6, pp. 724-732, 2018.
- [21] S. Tay and J. Marais, "Weighting models for GPS Pseudorange observations for land transportation in urban canyons," in *6th European Workshop on GNSS Signals and Signal Processing*, 2013, p. 4p.
- [22] M. Spangenberg, O. Julien, V. Calmettes, and G. Duchâteau, "Urban navigation system for automotive applications using HSGPS, inertial and wheel speed sensors," in *ENC-GNSS 2008, Conférence Européenne de la Navigation*, 2008.

- [23] Y. Hao and F. Shen, "A Low-cost IMU/GNSS Cooperative Positioning Method for VANETs in the Urban Environments," *International Journal of Smart Home*, vol. 9, no. 12, pp. 255-266, 2015.
- [24] W. W. Zhang G., Hsu, L.T., "Rectification of GNSS based Collaborative Positioning using 3D Building Models in Urban Areas," *GPS Solutions*, 2019.
- [25] L.-T. Hsu, F. Chen, and S. Kamijo, "Evaluation of multi-GNSSs and GPS with 3D map methods for pedestrian positioning in an urban canyon environment," *IEICE Transactions on Fundamentals of Electronics, Communications and Computer Sciences*, vol. 98, no. 1, pp. 284-293, 2015.
- [26] L.-T. Hsu, Y. Gu, Y. Huang, and S. Kamijo, "Urban pedestrian navigation using smartphone-based dead reckoning and 3-D map-aided GNSS," *IEEE Sensors Journal*, vol. 16, no. 5, pp. 1281-1293, 2016.
- [27] L.-T. Hsu, Y. Gu, and S. Kamijo, "3D building model-based pedestrian positioning method using GPS/GLONASS/QZSS and its reliability calculation," *GPS solutions*, vol. 20, no. 3, pp. 413-428, 2016.
- [28] S. Miura, L.-T. Hsu, F. Chen, and S. Kamijo, "GPS error correction with pseudorange evaluation using three-dimensional maps," *IEEE Transactions on Intelligent Transportation Systems*, vol. 16, no. 6, pp. 3104-3115, 2015.
- [29] H. F. Ng, Zhang, G., Hsu, L.-T, "Range-based 3D Mapping Aided GNSS with NLOS Correction based on Skyplot with Building Boundaries," presented at the ION Pacific PNT, Honolulu, Hawaii, 2019.
- [30] J. S. Sánchez, A. Gerhmann, P. Thevenon, P. Brocard, A. B. Afia, and O. Julien, "Use of a FishEye camera for GNSS NLOS exclusion and characterization in urban environments," in *ION ITM 2016, International Technical Meeting*, 2016: ION.
- [31] S. Kato, M. Kitamura, T. Suzuki, and Y. Amano, "Nlos satellite detection using a fish-eye camera for improving gnss positioning accuracy in urban area," *Journal of robotics and mechatronics*, vol. 28, no. 1, pp. 31-39, 2016.
- [32] L. Wang, P. D. Groves, and M. K. Ziebart, "Urban positioning on a smartphone: Real-time shadow matching using GNSS and 3D city models," 2013: The Institute of Navigation.
- [33] L. Wang, P. D. Groves, and M. K. Ziebart, "GNSS shadow matching: Improving urban positioning accuracy using a 3D city model with optimized visibility scoring scheme," *Navigation*, vol. 60, no. 3, pp. 195-207, 2013.
- [34] L. Wang, P. D. Groves, and M. K. Ziebart, "Smartphone shadow matching for better cross-street GNSS positioning in urban environments," *The Journal of Navigation*, vol. 68, no. 3, pp. 411-433, 2015.
- [35] P. D. Groves and M. Adjrad, "Likelihood-based GNSS positioning using LOS/NLOS predictions from 3D mapping and pseudoranges," *GPS Solutions*, journal article vol. 21, no. 4, pp. 1805-1816, October 01 2017.
- [36] M. Adjrad and P. D. Groves, "Intelligent Urban Positioning: Integration of Shadow Matching with 3D-Mapping-Aided GNSS Ranging," *Journal of Navigation*, vol. 71, no. 1, pp. 1-20, 2018.
- [37] L.-T. Hsu, Y. Gu, and S. Kamijo, "3D building model-based pedestrian positioning method using GPS/GLONASS/QZSS and its reliability calculation," (in English), *GPS Solutions*, vol. 20, no. 3, pp. 413-428, 2016.
- [38] M. Obst, S. Bauer, P. Reisdorf, and G. Wanielik, "Multipath detection with 3D digital maps for robust multi-constellation GNSS/INS vehicle localization in urban areas," in *Intelligent Vehicles Symposium (IV), 2012 IEEE*, 2012, pp. 184-190: IEEE.
- [39] T. Suzuki and N. Kubo, "Correcting GNSS multipath errors using a 3D surface model and particle filter," *Proc. ION GNSS+ 2013*, 2013.
- [40] J. I. Meguro, T. Murata, J. I. Takiguchi, Y. Amano, and T. Hashizume, "GPS multipath mitigation for urban area using omnidirectional infrared camera," *IEEE Transactions on Intelligent Transportation Systems*, vol. 10, no. 1, pp. 22-30, 2009.
- [41] T. Suzuki, M. Kitamura, Y. Amano, and T. Hashizume, "High-accuracy GPS and GLONASS positioning by multipath mitigation using omnidirectional infrared camera," in *IEEE International Conference on Robotics and Automation*, 2011, pp. 311-316.
- [42] W. X., W., Zhang, G., Hsu, Li-Ta, "Real-time GNSS NLOS Detection and Correction Aided by Sky-Pointing Camera and 3D LiDAR," presented at the Proceedings of ION Pacific PNT 2019, Honolulu, HA, USA, 2019.
- [43] P. V. Gakne, "Improving the Accuracy of GNSS Receivers in Urban Canyons using an Upward-Facing Camera," PhD Thesis, Geomatics Engineering, University of Calgary. doi: dx. doi. org ..., 2018.
- [44] P. V. Gakne and K. O'Keefe, "Tightly-Coupled GNSS/Vision Using a Sky-Pointing Camera for Vehicle Navigation in Urban Areas," *Sensors*, vol. 18, no. 4, p. 1244, 2018.
- [45] R. Mur-Artal, J. M. M. Montiel, and J. D. Tardos, "ORB-SLAM: a versatile and accurate monocular SLAM system," *IEEE Transactions on Robotics*, vol. 31, no. 5, pp. 1147-1163, 2015.
- [46] W. Wen, Zhang, G., Hsu, Li-Ta, "Correcting GNSS NLOS by 3D LiDAR and Building Height," presented at the ION GNSS+, 2018, Miami, Florida, USA, 2018.
- [47] T. Takasu and A. Yasuda, "Development of the low-cost RTK-GPS receiver with an open source program package RTKLIB," in *International symposium on GPS/GNSS*, 2009, pp. 4-6: International Convention Center Jeju Korea.
- [48] J. Marshall, "Creating and viewing skyplots," *GPS solutions*, vol. 6, no. 1-2, pp. 118-120, 2002.
- [49] G. Bradski and A. Kaehler, "OpenCV," *Dr. Dobb's journal of software tools*, vol. 3, 2000.

- [50] J. Kannala and S. S. Brandt, "A generic camera model and calibration method for conventional, wide-angle, and fish-eye lenses," *IEEE transactions on pattern analysis and machine intelligence*, vol. 28, no. 8, pp. 1335-1340, 2006.
- [51] E. Kaplan and C. Hegarty, *Understanding GPS: principles and applications*. Artech house, 2005.
- [52] P. Misra and P. Enge, "Global Positioning System: signals, measurements and performance second edition," *Massachusetts: Ganga-Jamuna Press*, 2006.
- [53] A. M. Herrera, H. F. Suhandri, E. Realini, M. Reguzzoni, and M. C. de Lacy, "goGPS: open-source MATLAB software," *GPS solutions*, vol. 20, no. 3, pp. 595-603, 2016.
- [54] T. D. Barfoot, *State Estimation for Robotics*. Cambridge University Press, 2017.
- [55] S. Thrun, W. Burgard, and D. Fox, *Probabilistic robotics*. MIT press, 2005.
- [56] G. Wan, X. Yang, R. Cai, H. Li, H. Wang, and S. Song, "Robust and Precise Vehicle Localization based on Multi-sensor Fusion in Diverse City Scenes," *arXiv preprint arXiv:1711.05805*, 2017.
- [57] F. Dellaert, "Factor graphs and GTSAM: A hands-on introduction," Georgia Institute of Technology 2012.
- [58] M. Quigley *et al.*, "ROS: an open-source Robot Operating System," in *ICRA workshop on open source software*, 2009, vol. 3, no. 3.2, p. 5: Kobe, Japan.

The Hong Kong Polytechnic University. His research interests are on Lidar based localization in challenging areas for autonomous vehicles and evaluating the effect of dynamic objects on map based localization methods.



Li-Ta Hsu received the B.S. and Ph.D. degrees in aeronautics and astronautics from National Cheng Kung University, Taiwan, in 2007 and 2013, respectively. He is currently an assistant professor with Interdisciplinary Division of Aeronautical and Aviation Engineering, The Hong Kong Polytechnic University, before he served as post-doctoral researcher in Institute of Industrial Science at University of Tokyo, Japan. In 2012, he was a visiting scholar in University College London, U.K. His research interests include GNSS positioning in challenging environments and localization for pedestrian, autonomous driving vehicle and unmanned aerial vehicle.



Weisong Wen was born in Ganzhou, Jiangxi, China. He is a Ph.D. candidate in mechanical engineering, the Hong Kong Polytechnic University. His research interests include multi-sensor integrated localization for autonomous vehicles, SLAM and GNSS positioning. He was a visiting student researcher in University of California, Berkeley (UCB) in 2018.



Xiwei Bai is currently a research assistant with Interdisciplinary Division of Aeronautical and Aviation Engineering, in Hong Kong Polytechnic University. Her research topic is GNSS positioning aided by computer vision, object detection and recognition using deep neural network.



Yin Chiu Kan was born in Hong Kong, China. He received his Bachelor and Master of Science in Aerospace Engineering at University of Maryland, College Park. He is currently working as an assistant technical officer in Interdisciplinary Division of Aeronautical and Aviation Engineering,